American Mineralogist, Volume 92, pages 1685–1694, 2007

Non-ideality and defectivity of the åkermanite-gehlenite solid solution: An X-ray diffraction and TEM study

Mauro Gemmi,[1,*] Marco Merlini,[1] Giuseppe Cruciani,[2] and Gilberto Artioli[1]

[1]Dipartimento di Scienze della Terra "A. Desio," Università degli Studi di Milano, via Botticelli, 23, I-20133 Milano, Italy
[2]Dipartimento di Scienze della Terra, Università di Ferrara, via Saragat 1, I-44100 Ferrara, Italy

Abstract

This paper reports a structure analysis of the åkermanite-gehlenite solid solution. This solution is non-ideal with a negative excess volume in the entire compositional range. X-ray diffraction shows anomalous behavior of the cell parameters close to the gehlenite end-member ($åk_{08}ge_{92}$, $åk_{35}ge_{65}$). This behavior is correlated with an excess of Si and deficiency of Al with respect to the Mg content, which implies a defective, non-stoichiometric structure with Ca vacancies. Electron microscopy images have confirmed an increase in the defectivity on the atomic scale for Al-rich compositions, and single-crystal structure refinements show a correlated decrease of the tetrahedral volume preferentially occupied by Si. The incommensurate modulation, characteristic of åkermanite, has been observed also in $åk_{95}ge_{05}$, and it is still visible as diffuse scattering in $åk_{75}ge_{25}$. (210) twinning has been observed in the entire compositional range.

Keywords: Melilite, solid solution, X-ray diffraction, electron microscopy

Introduction

Melilites are characteristic constituents of both ultramafic plutonic (alnöite) and ultramafic extrusive (melilitites) rocks. In metamorphic rocks, they appear in metamorphosed siliceous dolomites (Yoder 1973). They also occur in the Ca-Al inclusions (CAI) of carbonaceous chondrites and are considered to be among the first silicate minerals to have crystallized from the solar nebula (Wood 1988). As synthetic materials, melilites are also common components of industrial slag, clinkers, and technological glasses (Taylor 1997). Their chemical composition is highly variable. They are solid solutions among the gehlenite (ge, $Ca_2Al_2SiO_7$), åkermanite (åk, $Ca_2MgSi_2O_7$), soda-melilite (sm, $NaCaAlSi_2O_7$), and Fe-bearing end-members (Fe^{3+}-gehlenite/Fe^{2+}-åkermanite) (Deer et al. 1992). Other important cations known to be hosted in the structure of natural samples are Zn for Mg in åkermanite, giving the mineral hardystonite (Louisnathan 1969), and Sr replacing Ca in soda-melilite (Bindi et al. 2001). Minerals with a similar structure include okayamalite $Ca_2SiB_2O_7$ (Giuli et al. 2000) and gugiaite $Ca_2BeSi_2O_7$ (Peng et al. 1962; Kimata and Ohashi 1982) (see Table 1). The melilite structure is tetragonal, space group $P\bar{4}2_1m$, and it was first determined by Warren (1930). The melilite structure can be described as layers of corner-sharing oxygen tetrahedra centered by Mg, Al, and Si connected to form five-membered rings. Calcium and Na cations are located between the layers in eightfold coordination, centering a distorted square antiprism oxygen polyhedron. The layers are formed by two non-equivalent tetrahedra, T_1 located at the origin, and T_2 located on (110) mirror planes, which are preferentially occupied by different cations. Kimata and Ii (1981) showed that in åkermanite, T_1 is mainly occupied by Mg and T_2 by Si, as predicted on the basis of the polyhedral size (Smith 1953). Smith also proposed two possible schemes for Al substitution along the åk-ge join giving two possible gehlenite structures: one with T_1 fully occupied by Al and with a mixed occupancy ($Al_{0.5}Si_{0.5}$) of T_2, and a second one with T_1 fully occupied by Si and T_2 fully occupied by Al. Louisnathan (1971) demonstrated that in gehlenite the first model is the correct one, whereas in soda melilite, T_1 is occupied solely by Al and T_2 by Si (Louisnathan 1970). Later Waldbaum and Woodhead (1975) proposed possible ordered structures in the melilite solid solutions. They proposed a relation between the cation order and the variation of the unit-cell parameters and discussed the influence of the thermal history on ordering.

Since the discovery by Hemingway et al. (1986) and Seifert et al. (1987) of the occurrence of a phase transition from an incommensurately modulated to a normal structure in åkermanite, several papers focused on this subject have appeared. In contrast, systematic investigations of the structural properties of the åk-ge solid solution are still scarce. Charlu et al. (1981) focused on calorimetric studies and reported that the åk-ge solid solution is close to ideal. They studied samples synthesized from glass and from solid-state reactions. Using powder X-ray diffraction (XRD), they observed a negative excess volume over the entire solid solution. Swainson et al. (1992) performed a detailed neutron powder diffraction study on three melilite samples of intermediate composition ($åk_{25}$, $åk_{50}$, $åk_{75}$) and on the end-members. All samples were synthesized by annealing glasses at 1523 K, and the chemical composition was assumed from the chemical analysis of the starting glasses. The tetrahedral site occupancies

* E-mail: mauro.gemmi@unimi.it

0003-004X/07/0010–1685$05.00/DOI: 10.2138/am.2007.2380

TABLE 1. Unit-cell parameters and volumes of the minerals having melilite structure

Mineral name	Chemical formula	*a* (Å)	*c* (Å)	*V* (Å^3)	Reference
Åkermanite	$Ca_2MgSi_2O_7$	7.8288(8)	5.0052(2)	306.77(6)	Swainson et al. 1992
Gehlenite	$Ca_2Al_2SiO_7$	7.6850(4)	5.0636(3)	299.05(5)	Swainson et al. 1992
Na-melilite	$CaNaAlSi_2O_7$	7.6344(6)	5.0513(6)	294.41(6)	Louisnathan 1970
Hardystonite	$Ca_2ZnSi_2O_7$	7.828(1)	5.0138(6)	307.23(7)	Louisnathan 1969
Okayamalite	$Ca_2SiB_2O_7$	7.1248(2)	4.8177(2)	244.56(1)	Giuli et al. 2000
Gugiaite	$Ca_2BeSi_2O_7$	7.419(1)	4.988(1)	274.6(1)	Kimata and Ohashi 1982

of T_1 and T_2 were deduced from the refinement of the average neutron scattering lengths. The authors confirmed that Mg occupies preferentially the T_1 site and also derived a relationship between the cell parameters and the tilt of the tetrahedra describing the non-ideality of the solid solution.

The present study is part of a project aimed at understanding the thermal properties of melilite solid solutions along the åk-ge join. Results concerning the thermal expansion and the structural modifications on heating will be presented in an additional paper (Merlini et al. submitted). While performing the preliminary characterization of melilite samples obtained from two different synthesis methods (as illustrated below), we found an anomalous behavior of the cell parameters with respect to the chemical compositions of synthesized samples. The aim of the present paper is to understand the origin of such an anomalous behavior by combining unit-cell measurements, crystal-structure analysis, and chemical compositions determined on two series of samples synthesized in the åk-ge join. Synchrotron powder diffraction and single-crystal X-ray diffraction have been used for accurate unit-cell determination and structure refinement, respectively. The samples were also characterized by transmission electron microscopy (TEM) to evaluate their defects and to seek structural details not visible by the X-ray analysis.

EXPERIMENTAL METHODS

Synthetic samples

The samples along the åk-ge join were synthesized by two methods from a mixture of pure oxides (MgO, CaO, SiO_2, Al_2O_3), weighed in the appropriate stoichiometric ratio.

Synthesis 1 (S1). Samples were melted at 1923 K and then crystallized by annealing for 8 h at 1323 K. These samples have the compositions: $åk_{100}$, $åk_{90}ge_{10}$, $åk_{75}ge_{25}$, $åk_{54}ge_{46}$, $åk_{35}ge_{65}$, $åk_{08}ge_{92}$, ge_{100} determined by EDS on powder samples and with EMPA-WDS on single crystals.

Synthesis 2 (S2). Samples were crystallized for 3 h at temperatures just below the solidus, following the phase diagram of Osborn and Shairer (1941). The crystallizing temperatures were 1708, 1698,1643, 1648, 1698, 1773, and 1833 K for the compositions $åk_{100}$, $åk_{95}ge_{05}$, $åk_{75}ge_{25}$, $åk_{50}ge_{50}$, $åk_{25}ge_{75}$, $åk_{10}ge_{90}$, ge_{100}, respectively. The mixtures of oxides were then compressed and heated for 4 h at 1550 K. The samples were ground and re-compressed and the procedure was repeated several times before a final annealing for 24 h at 1500 K. The final compositions were checked with EDS on powder samples.

Synthesis S1 gave samples suitable for single-crystal XRD studies, whereas synthesis S2 yielded powder samples only.

Powder and single-crystal XRD

Single-crystal XRD was carried out on a kappa four-circle Oxford X'calibur diffractometer, equipped with a CCD detector and a Mo X-ray source. Data were collected with ϕ- and ω-scans having an angular step of 1° and a counting time of 10–20 s. The full Ewald sphere was acquired, with a redundancy of data suitable for applying an empirical absorption correction using the Blessing method (Blessing 1995). Data were processed with the Crysalis software (Oxford 2003). Accurate unit-cell measurements were performed from single-crystal and powder XRD data on the same samples, using Si standard (NIST 640c) for accurate zero diffractometer calibration. Powder XRD was performed on a Philips X'pert θ–θ diffractometer.

The samples S2 have been characterized by synchrotron powder XRD at the Italian CRG beamline BM08 (GILDA) at ESRF, Grenoble. Samples were filled to 0.5 mm quartz capillaries. The wavelength was set to 0.55133(1) Å and the data were recorded with a Fuji Image Plate. The sample to detector distance was 232.70 mm, calibrated on a LaB_6 standard (NIST SRM 660b), allowing data collection up to 50 °2θ, which corresponds to a resolution of 0.65 Å. The scanned images were integrated using the program Fit2D (Hammersley et al. 1996).

Structures were refined with the Jana2000 program (Petricek and Dusek 2000) for single-crystal data, and with GSAS (Larson and Von Dreele 1988) for powder diffraction data. The results of the structure refinements are summarized in Tables 2, 3, 4, and 5. For brevity we have reported the atomic positions, the anisotropic thermal parameters, the distances, and the angles only for the single-crystal refinements. The structural parameters obtained from powder refinements are reported in the figures only.

EMPA and EDS

EMPA analyses were carried out on an Applied Research Laboratories (ARL) SEMQ instrument at the Earth Science Department, University of Milan. The analyses were performed on the same crystals that were used for single-crystal XRD measurements as well as on several other crystals from the same synthesis batch to check for compositional variability. Rim and core portions of large crystals were analyzed separately to assess possible zoning.

Transmission electron microscopy

Samples for transmission electron microscopy (TEM) were prepared by mild grinding in an agate mortar, suspension in ethanol, and deposition on Cu grids covered by a holey carbon film. TEM observations were carried out on a field-emission-gun FEI Tecnai F20 super twin electron microscope equipped with a Gatan Slow Scan 794 CCD camera at the Earth Science Depertment, University of Milan.

RESULTS

Single-crystal and powder X-ray diffraction

The variations of the unit-cell volume across the åk-ge join are reported in Figure 1 (top) as a function of åk%, calculated from the Mg content measured by EMPA. Data measured on single crystals (series S1) are compared with those obtained from powder samples (series S2). The variations along the join are similar in both series, showing a moderate deviation from linearity, which is slightly larger in the case of S1. In terms of excess volume, both S1 and S2 appear to be non-ideal. To quantify the excess volume we recall that the åk-ge join cannot be considered as a complete solid-solution series because, at room temperature, åk has a modulated structure and therefore the åk molar volume cannot be used as the reference for the Mg end-member. For a proper check of Vegard's law across the join, the extrapolation to room temperature of the åk high-temperature normal phase molar volume V_n must instead be chosen as the reference. Using the thermal expansion data published by Merlini et al. (2005a), we obtained $V_n = 307.5468$ Å^3. The corresponding excess volumes shown in Figure 1 (bottom) indicate that both S1 and S2 exhibit negative excess molar volumes along the entire compositional range.

Figure 2 shows the variation of the unit-cell parameters across

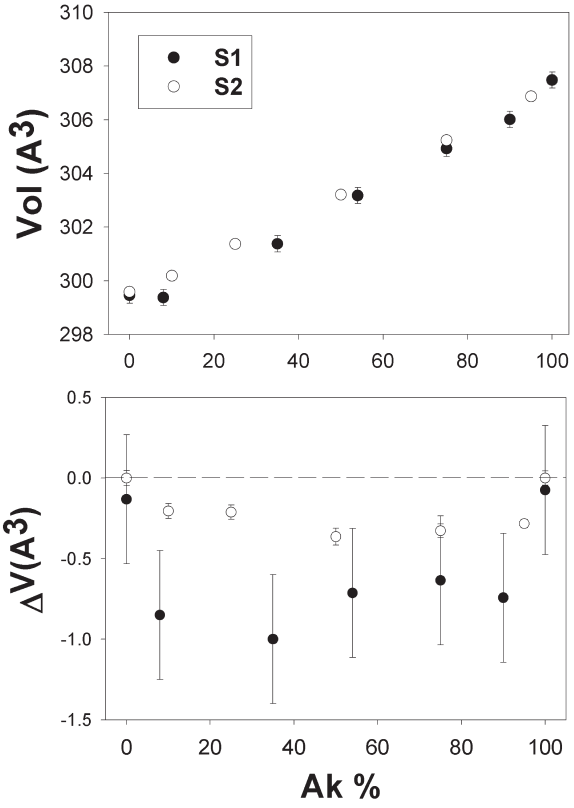

FIGURE 1. Variation of the unit-cell volume (**top**) and of the excess molar volume (**bottom**) across the åk-ge solid solution for the syntheses S1 and S2. The error bars, if not reported, are smaller than the symbols.

TABLE 2. Details of the structure refinements of both syntheses

Åk%	0	8	35	54	75	90	100
			S1				
R [for $F_o > 3s(F_o)$]	3.07	2.99	4.17	2.84	2.42	4.21	4.17
Rw [for $F_o > 3s(F_o)$]	6.12	2.87	3.61	2.87	3.04	3.74	4.4
R (for all F_o)	3.55	3.84	7.51	3.56	2.46	5.66	4.42
Rw (for all F_o)	6.2	3.03	4.23	2.99	3.05	4.04	4.44
GoF [for $F_o > 3s(F_o)$]	3.32	1.22	1.19	1.25	1.78	1.57	2.91
$F_o > 3s(F_o)$	9411	18153	13879	18727	19859	7859	9515
Independent refl.	339	541	539	541	531	342	342
R_{merge}	3.0	3.8	6.7	3.5	2.3	3.9	2.0
			S2				
Åk%	0	10	25	50	75	95	100
wR_p	10.4	5.22	6.59	6.16	6.45	8.21	6.87
R_p	7.02	3.65	4.53	4.19	4.42	5.37	4.6
RF^2	8.66	5.5	6.39	6.63	7.72	8.02	8.08
R_{bragg}	4.79	3.7	4.82	4.79	5.21	5.72	5.73

Notes: Crystal system = tetragonal; Space group = $P\bar{4}2_1m$. For S1 single-crystal refinements the agreement factors produced by program JANA2000 are reported together with the details of the data collection. For S2 powder diffraction refinements the agreement factors are reported.

the åk-ge join. From åk to ge, the *a* parameter shrinks while *c* expands, a behavior that is well documented. This anisotropy is due to the fact that *a* and *c* are controlled by the size of two different polyhedra: T_1 controls *a,* and T_2 controls *c*. Since in åk T_1 is fully occupied by Mg, the substitution Mg ↔ Al and Si ↔ Al has an opposite effect on the two polyhedral sizes, and consequently on the unit-cell parameters (Waldbaum and Woodhead

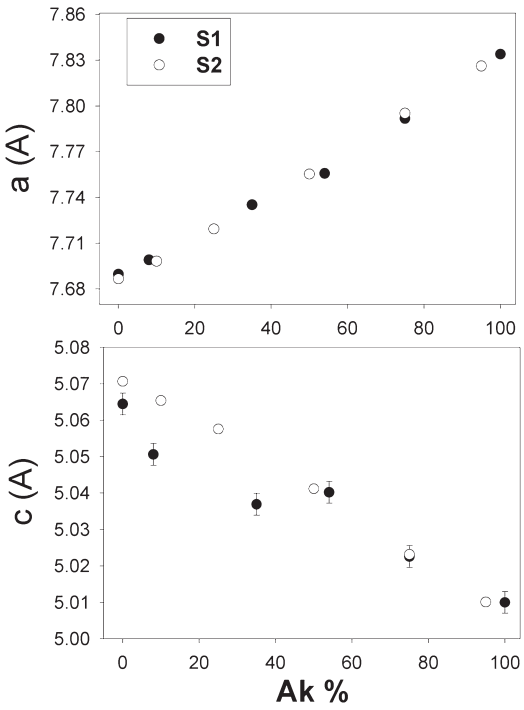

FIGURE 2. Variation of the unit-cell parameters across the åk-ge solid solution for the synthesis S1 and S2. The error bars, if not reported, are smaller than the symbols.

TABLE 3. Unit-cell parameters and volumes for both syntheses

	S1			S2		
Åk%	*a*	*c*	*V*	*a*	*c*	*V*
0	7.690(2)	5.064(2)	299.5(4)	7.6866(3)	5.0707(3)	299.60(4)
8	7.699(2)	5.051(2)	299.4(4)			
10				7.6982(3)	5.0654(3)	300.19(4)
25				7.7193(3)	5.0576(3)	301.37(4)
35	7.735(2)	5.037(2)	301.4(4)			
54	7.748(2)	5.041(2)	303.2(4)			
50				7.7554(3)	5.0412(3)	303.21(4)
75	7.792(2)	5.023(2)	304.9(4)	7.7952(3)	5.0232(3)	305.23(4)
90	7.812(2)	5.014(2)	306.0(4)			
95				7.8262(3)	5.0101(3)	306.87(4)
100	7.834(2)	5.010(2)	307.5(4)	7.8258(3)	5.0085(3)	306.73(4)

1975). The substitution of Mg for Al in T_1 is responsible for a decrease of the tetrahedral layer thickness by shifting the O2 oxygen that belong to T_2 and define the layer thickness, closer to the T_2 cation site.

A comparison of the *a* and *c* cell lengths shows differences between the S1 and S2 samples. In the S2 series, *a* and *c* vary almost linearly with composition. In contrast, in the S1 series, *c* shows a departure from linear behavior between $åk_{50}$ and ge, whereas *a* follows the same trend as S2 over the entire åk-ge range. To ensure that this effect was not due to the lower accuracy in the unit-cell determination by the single-crystal diffractometer, we performed powder measurements on ground single crystals obtained in the S1 synthesis. The unit-cell parameters obtained in this way were identical, within error, to unit-cell determinations using single-crystal XRD. An anomalous behavior is also

TABLE 4. Atomic positions and equivalent isotropic thermal parameters (in Å^2) for S1 single-crystal refinements

		0	8	35	54	75	90	100
Ca	x	0.33876(2)	0.339107(10)	0.337639(16)	0.336167(9)	0.335022(9)	0.33305(2)	0.33172(3)
Ca	y	0.16124(2)	0.160893(10)	0.162361(16)	0.163833(9)	0.164978(9)	0.16695(2)	0.16828(3)
Ca	z	0.51145(5)	0.51153(2)	0.51055(4)	0.50962(2)	0.50851(2)	0.50695(6)	0.50643(6)
Ca	U_{eq}	0.01691(6)	0.01448(2)	0.01693(4)	0.01574(2)	0.01424(2)	0.02120(6)	0.01967(8)
T1	x	0	0	0	0	0	0	0
T1	y	0	0	0	0	0	0	0
T1	z	0	0	0	0	0	0	0
T1	Mg/Al occ	0/1	0.08/0.92	0.35/0.65	0.54/0.46	0.75/0.25	0.9/0.1	1/0
T1	U_{eq}	0.00942(12)	0.00918(4)	0.01040(8)	0.00920(4)	0.00793(5)	0.01433(13)	0.01085(14)
T2	x	0.14327(4)	0.142434(14)	0.14182(2)	0.141662(13)	0.140757(12)	0.14044(3)	0.13986(3)
T2	y	0.35673(4)	0.357566(14)	0.35818(2)	0.358338(13)	0.359243(12)	0.35956(3)	0.36014(3)
T2	z	0.95662(7)	0.95207(3)	0.94738(5)	0.94542(3)	0.93988(2)	0.93718(6)	0.93540(7)
T2	Ueq	0.00836(8)	0.00719(3)	0.00961(5)	0.00887(3)	0.00725(2)	0.01426(8)	0.00958(8)
T2	Si/Al occ	0.5/0.5	0.54/0.46	0.625/0.375	0.77/0.23	0.875/0.125	0.95/0.05	1/0
O1	x	0.5	0.5	0.5	0.5	0.5	0.5	0.5
O1	y	0	0	0	0	0	0	0
O1	z	0.1765(2)	0.17825(12)	0.1788(2)	0.17920(11)	0.17969(13)	0.1802(3)	0.1810(3)
O1	U_{eq}	0.0114(3)	0.01667(13)	0.0188(2)	0.01998(13)	0.02027(9)	0.0246(3)	0.0237(4)
O2	x	0.14339(9)	0.14430(4)	0.14313(6)	0.14194(4)	0.14225(4)	0.14085(9)	0.14094(10)
O2	y	0.35661(9)	0.35570(4)	0.35687(6)	0.35806(4)	0.35775(4)	0.35915(9)	0.35906(10)
O2	z	0.28295(14)	0.27621(7)	0.26788(13)	0.26795(7)	0.26166(8)	0.25520(16)	0.25384(19)
O2	U_{eq}	0.0136(2)	0.01528(8)	0.01886(16)	0.01826(8)	0.01704(6)	0.0230(2)	0.0215(3)
O3	x	0.08739(8)	0.08899(4)	0.08666(6)	0.08488(4)	0.08391(5)	0.08206(9)	0.08095(13)
O3	y	0.16685(9)	0.16905(4)	0.17382(7)	0.17605(4)	0.18094(4)	0.18440(9)	0.18667(11)
O3	z	0.80582(13)	0.80524(6)	0.80018(11)	0.79709(6)	0.79232(6)	0.78884(14)	0.78658(17)
O3	U_{eq}	0.0128(2)	0.01632(9)	0.02008(16)	0.02029(9)	0.01950(6)	0.0259(2)	0.0257(3)

TABLE 5. Anisotropic thermal parameters derived from S1 single-crystal refinements

		0	8	35	54	75	90	100
Ca	$U_{11} = U_{22}$	0.01970(9)	0.01664(3)	0.01886(5)	0.01812(3)	0.01669(3)	0.02414(9)	0.02242(12)
	U_{33}	0.01132(12)	0.01017(4)	0.01307(9)	0.01098(4)	0.00989(3)	0.01532(12)	0.01417(15)
	U_{12}	0.00933(13)	0.00664(4)	0.00566(8)	0.00640(4)	0.00624(3)	0.00802(13)	0.01235(12)
	$U_{13} = -U_{23}$	0.00109(10)	0.00106(3)	0.00132(6)	0.00108(3)	0.001491(18)	0.00165(9)	0.00186(9)
T1	$U_{11} = U_{22}$	0.00762(16)	0.00765(6)	0.00899(10)	0.00794(6)	0.00730(5)	0.01422(18)	0.01071(19)
	U_{33}	0.0130(3)	0.01223(10)	0.0132(2)	0.01173(10)	0.00905(7)	0.0145(3)	0.0111(3)
	$U_{12} = U_{13} = U_{23}$	0	0	0	0	0	0	0
T2	$U_{11} = U_{22}$	0.00737(11)	0.00685(4)	0.00897(6)	0.00861(4)	0.00761(3)	0.01474(11)	0.00928(12)
	U_{33}	0.01033(19)	0.00785(6)	0.01089(13)	0.00940(6)	0.00642(4)	0.01329(18)	0.01018(17)
	U_{12}	−0.00065(17)	−0.00020(5)	−0.00007(9)	0.00030(5)	0.00064(4)	0.00031(16)	0.00146(14)
	$U_{13} = -U_{23}$	0.00011(12)	0.00015(4)	0.00045(7)	0.00019(3)	0.00020(2)	0.00064(10)	0.00102(10)
O1	$U_{11} = U_{22}$	0.0138(5)	0.01888(19)	0.0229(3)	0.0249(2)	0.02637(16)	0.0316(6)	0.0312(6)
	U_{33}	0.0064(7)	0.0122(3)	0.0107(5)	0.0101(3)	0.00807(17)	0.0105(7)	0.0087(7)
	U_{12}	−0.0009(6)	−0.0028(2)	−0.0065(5)	−0.0122(3)	−0.0165(2)	−0.0120(8)	−0.0220(8)
	$U_{13} = U_{23}$	0	0	0	0	0	0	0
O2	$U_{11} = U_{22}$	0.0144(3)	0.01589(12)	0.0205(2)	0.01952(13)	0.01997(10)	0.0288(4)	0.0263(4)
	U_{33}	0.0121(4)	0.01405(16)	0.0155(3)	0.01574(17)	0.01120(11)	0.0115(4)	0.0118(5)
	U_{12}	0.0019(5)	0.00155(19)	0.0027(4)	0.00451(19)	0.00500(16)	0.0086(6)	0.0132(6)
	$U_{13} = -U_{23}$	−0.0021(3)	−0.00166(11)	−0.0016(2)	−0.00212(11)	−0.00195(7)	−0.0003(3)	−0.0010(3)
O3	U_{11}	0.0210(4)	0.02194(17)	0.0269(3)	0.02760(18)	0.02825(12)	0.0398(5)	0.0468(6)
	U_{22}	0.0072(4)	0.01225(15)	0.0171(3)	0.01726(16)	0.01532(11)	0.0198(4)	0.0132(4)
	U_{33}	0.0102(3)	0.01477(13)	0.0163(3)	0.01601(13)	0.01492(9)	0.0180(4)	0.0173(4)
	U_{12}	−0.0028(3)	−0.00338(13)	−0.0048(2)	−0.00560(13)	−0.00669(11)	−0.0079(4)	−0.0109(5)
	U_{13}	0.0045(3)	0.00484(11)	0.0040(2)	0.00469(12)	0.00593(9)	0.0058(3)	0.0099(4)
	U_{23}	−0.0005(3)	−0.00235(12)	−0.0038(2)	−0.00455(12)	−0.00459(9)	−0.0026(3)	−0.0025(3)

Notes: The thermal parameters are defined as $\exp(-2\pi^2\Sigma_i\Sigma_j U_{ij}h_ih_j\mathbf{a}_i^*\mathbf{a}_j^*)$ and are expressed in Å^2.

evident when plotting the fractional *z* coordinate of O2 oxygen vs. composition (Fig. 3, top). It is known that the fractional coordinates are not affected by the measured values of cell parameters; therefore, this is further evidence that the observed anomaly is not an artifact. In Figure 3 (bottom), we have also reported the surface roughness of the tetrahedral layer, which decreases with the åk content and is strongly correlated to the O2 *z* coordinate, which is the most variable among the coordinates of the O atoms.

The variations of the T_1, T_2, and Ca polyhedral volumes is another indicator of structural changes across the solid-solution series (see Fig. 4). As expected, the volume of T_1 decreases linearly from åk to ge for both syntheses. In S1, the volume of T_2 follows the same trend as *c*. In S2, the volume of T_2 is always larger than in S1, but for compositions from $åk_{50}$ to ge it deviates from linearity in a similar way. The S1 Ca polyhedron does not show a monotonic trend like the two previous polyhedra. Its volume decreases between åk and $åk_{75}$, shows a maximum for $åk_{35}$, and decreases again for Al-rich compositions (note that the Ca volume data for the S2 series are not reported because the errors coming from Rietveld refinement are too large). The polyhedral volume analysis shows that the cause of the anomalous *c* variation in S1 also affects samples S2, but in a less pronounced way. This difference becomes more evident if the deviation from the linear behavior of T_1, T_2, and Ca polyhedral volumes are plotted for both syntheses (Fig. 5). Though the absolute values are different, the volume of T_1 has a negative deviation in both data sets (difficult to see from the volume plot in Fig. 4 since the total

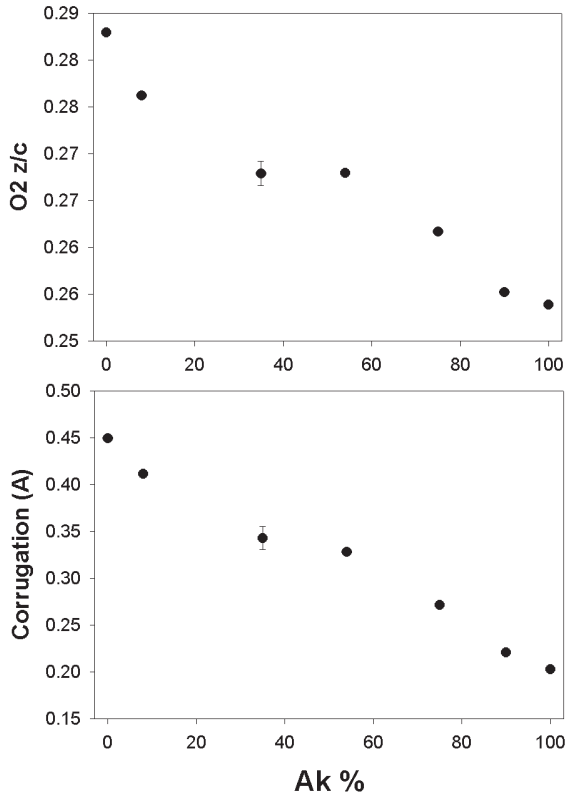

FIGURE 3. (**top**) Variation of the z coordinate of O2 vs. composition. (**bottom**) Corrugation of the tetrahedral layer expressed in angstroms as the difference between the z coordinates of O2 and O3.

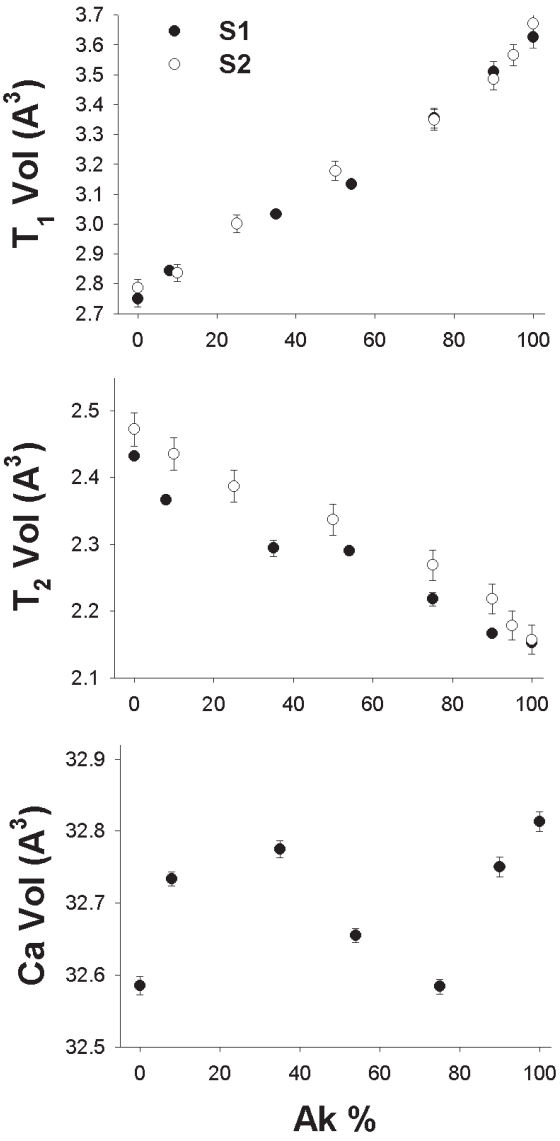

FIGURE 4. Variation of the T1, T2, and Ca polyhedral volumes across the åk-ge solid solution for the syntheses S1 and S2. The values of Ca volumes for S2 have not been shown since the errors are larger than the variation. The error bars, if not reported, are smaller than the symbols.

volume variation is quite big) in the interval $åk_{50}$-$åk_{100}$. The T_1 volume deviation becomes negligible or even positive between $åk_{50}$ and ge, whereas the largest negative deviation for the T_2 volume occurs in the $åk_{50}$-ge range. Further similarities between S1 and S2 series come from T_2-O distances (Fig. 6). The smaller T_2 volume in the S1 series compared to S2 is mainly due to the shorter distance between T_2 and O2, which is the only O atom of the T_2 tetrahedron not bonded to another cation of the T_3O_7 layer. However, in both syntheses, the T_2-O2 distance exhibits an anomalous decrease in the $åk_{50}$-ge range.

The modulation in åk is two dimensional in the *a*-*b* plane and has a displacive character. It involves mainly displacements of the O and the Ca atoms as can be inferred by the strong anisotropy of the O and Ca thermal ellipsoids. The results of the present structural refinements allow us to check whether the modulation and the IC to normal phase transition have some bearing on the anomalous behavior of structural parameters described above. A suitable indicator of the modulation is given by the anisotropy of the thermal parameters of the Ca and the O atoms. The difference between the longest and the average of the two shortest semi-axes of the thermal ellipsoids gives rise to the anisotropy. We call this quantity d_{max} following Armbruster et al. (1990). In Figure 7, the variation of d_{max} with chemical composition for the atoms Ca, O1, O2, and O3 is reported. For all O atoms the anisotropy decreases from åk to ge, with the simultaneous disappearance of the modulation. In addition, the d_{max} of Ca decreases initially, and then stabilizes in the interval $åk_{75}$-$åk_{08}$ and it increases in ge.

EMPA analyses

The EMPA data (Table 6) reveal that the compositions of $åk_{35}$ and $åk_{08}$ are significantly richer in Si and poorer in Al with respect to ideal melilite stoichiometry. To our knowledge, this is the first report of such non-stoichiometry features in synthetic melilites along the åk-ge join. It should be noted, however, that in previous investigations the composition of the synthetic melilites was assumed as being the same of the batch compositions without a direct analysis by EMPA on the synthesized products.

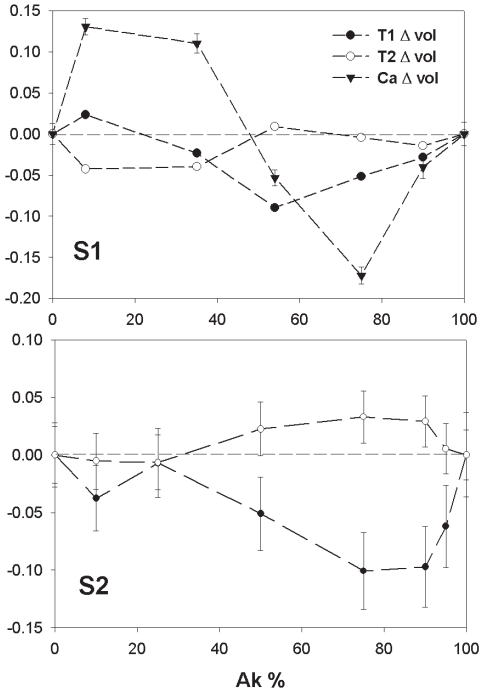

FIGURE 5. Deviation from linear behavior of the polyhedral volume for samples S1 (**top**) and S2 (**bottom**). The data are expressed in Å^3.

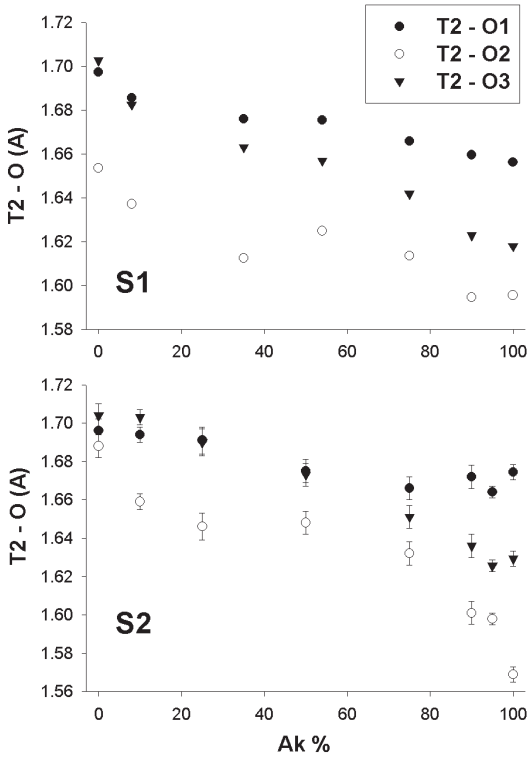

FIGURE 6. Plot of the distances between the O atoms and the T_2 site as a function of the sample composition for the synthesis S1 and S2. The error bars, if not reported, are smaller than the symbols.

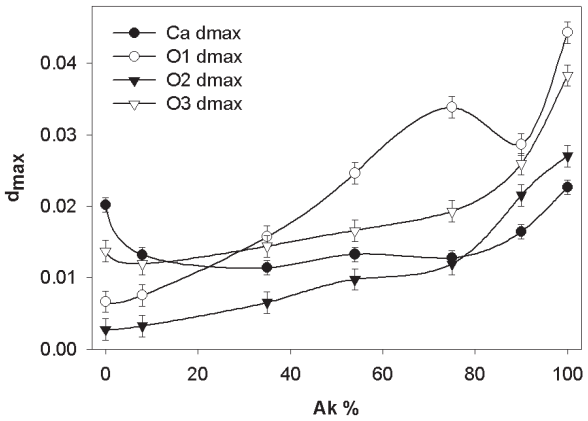

FIGURE 7. Plot of d_{max} variation across the join åk-ge for Ca, O1, O2, and O3. The d_{max} calculated for T_1 and T_2 sites have not been plotted since their anisotropy is negligible (d_{max}~0.005).

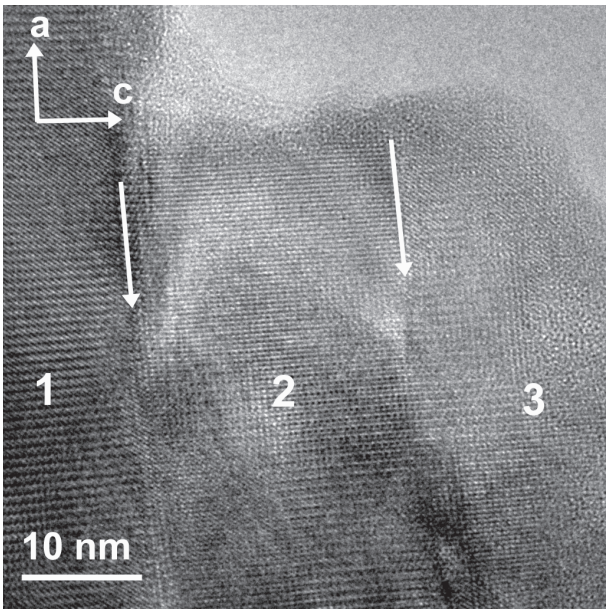

FIGURE 8. High-resolution electron image of åk$_{08}$ in [100] zone axis. Three different crystal grains are visible (1, 2, 3). The arrows indicate the grain boundaries that are approximately normal to the **c** axis. Every grain is slightly misaligned with respect to the other.

Transmission electron microscopy

The results of TEM analysis on the samples åk$_{35}$ and åk$_{08}$ have shown very small crystal grains slightly tilted with respect to one another but still retaining some precise crystallographic relation among them. A typical example is depicted in Figure 8, where three different grains in [100] orientation are visible. The grain boundaries are parallel to (001) and may indicate a concentration of defects on these planes. We do not have direct evidence for which kind of defects creates this mosaicism but TEM investigation on samples in the åk$_{50}$-åk$_{100}$ range have not shown this aspect.

Gehlenite has been reported to show lamellar and cross-

TABLE 6. Chemical analysis of the S1 single crystals used in the structure refinements

Åk%	100	90	75	54	35	8	0
Si	2.04 (2.00)	1.92 (1.90)	1.80 (1.75)	1.53 (1.54)	1.62 (1.35)	1.23 (1.08)	0.98 (1.00)
Mg	0.97 (1.00)	0.91 (0.90)	0.75 (0.75)	0.54 (0.54)	0.35 (0.35)	0.08 (0.08)	0.00 (0.0)
Al	0.00 (0)	0.19 (0.20)	0.52 (0.50)	0.93 (0.92)	1.00 (1.30)	1.67 (1.84)	2.05 (2.00)
Ca	1.95 (2.00)	1.97 (2.00)	1.86 (2.00)	2.00 (2.00)	1.91 (2.00)	1.96 (2.00)	1.96 (2.00)
Tot. Charge.	14.00	14.01	13.98	13.99	14.00	14.01	13.99

Notes: Compositions are given in atoms per formula unit based on 7 O atoms and are obtained from an average of 10 analysis points per crystal. The ideal composition based on the Mg content is reported in parentheses.

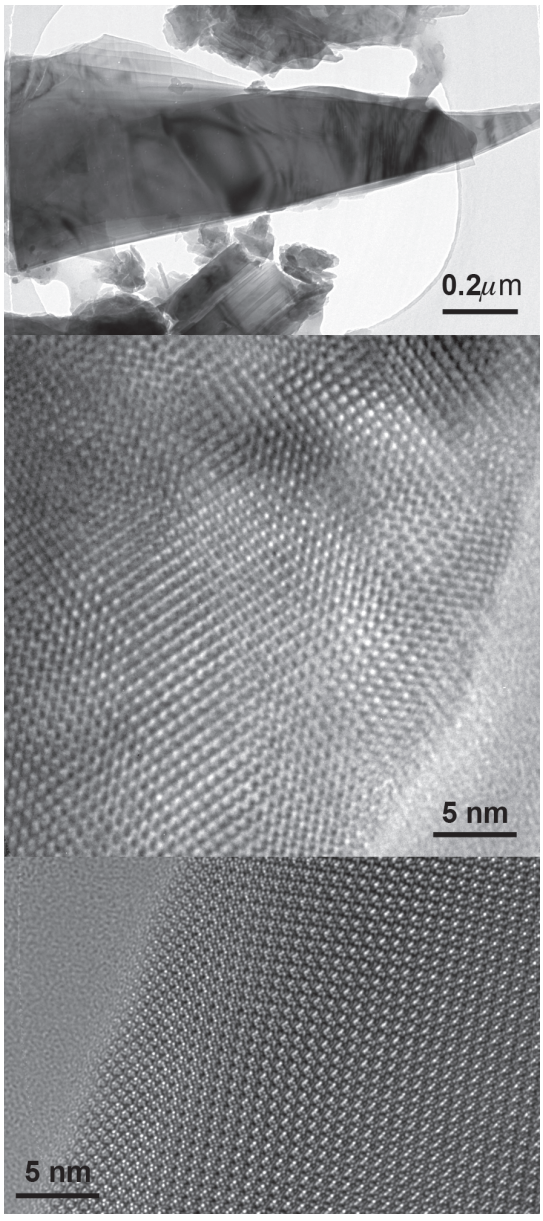

FIGURE 9. (**top**) Bright-field image of a crystal grain of ge, oriented in [001] zone axis. A lamellar character of the crystal shape is evident. (**middle**) High-resolution image of a crystal grain of ge, oriented in [001]. The crystal is highly strained as can be seen by the bending of the {100} crystallographic planes. (**bottom**) For comparison, an [001] high-resolution image of a well-crystallized $åk_{95}$ crystal is reported. The difference between the two images is evident.

hatched structure in thin section that was ascribed to microtwinning (Louisnathan 1971). This twinning would be caused by the Al/Si ordering in T_2 sites, which would make the ge structure triclinic. Our TEM observations of ge samples do not shown twinning due to reduced symmetry, but reveal a mosaicity on a smaller scale than $åk_{35}$ and $åk_{08}$. Several crystal grains were slightly bent on a scale of some hundred angstroms, and it was difficult to properly align a crystal in the microscope. In a normal bright-field image taken along [001] zone axis, the crystal grains appeared to be formed by several sheets stacked along the **c** axis (Fig. 9, top). High-resolution images show a highly strained structure (Fig. 9, center). The contrast varies irregularly over several nanometers, and the atomic details normally visible in well-crystallized melilites (see Fig. 9, bottom) are smeared out in strained crystals. Due to the lamellar crystal shape observed in bright-field images, this smearing can be interpreted as an imperfect stacking along **c** with small mismatching in the superposition of the layers. Unfortunately, it was not possible to record images of sufficiently good quality in the [100] orientation to confirm this interpretation.

The increase in defectivity as the ge end-member is approached has been confirmed by peak-shape analysis of powder XRD patterns collected at the synchrotron on S2 samples. The peak width increases for ge-rich compositions (Fig. 10), indicating either a reduced grain size or an increased number of defects and strain in the sample.

Synthetic and natural melilite samples commonly exhibit twinning, which must be duly taken into account when dealing with the structural characterization of melilite solid solutions. Twinning in melilite structures was first discovered in Cr- and B-doped synthetic gehlenite crystals by Panina et al. (1995) who also constructed a possible model. It has been classified as twinning by reticular polyholohedry by Nespolo and Ferraris (2004). The melilite twinning is characterized by a {210} twin plane formed by Ca, T_1, and O1 atoms. On opposite sides of this plane, the structure can grow with different chirality, giving rise to twins. The diffraction spots of the two individuals can be indexed on a superlattice having $a_T = b_T = 5^{1/2}a_I$, $c_T = c_I$, where the subscripts I and T indicate the individual lattice and the twin lattice respectively (Dapiaggi et al. 2002; Bindi et al. 2003). Due to the anomalous extinction conditions [only reflections hkl_T satisfying $2h + k = 0$ mod(5) or $h + 2k = 0$ mod(5) are observable], it is relatively easy to recognize it as twinning with X-ray diffraction. With electron diffraction, in contrast, it can be confused with a superstructure because, due to the relative orientation of the individuals, all the twin superlattice reflections hkl_T can be switched on by dynamical diffraction. In Figure 11, an $[001]_I$ electron diffraction pattern is displayed and all the twin lattice reflections are clearly visible. This can be explained only

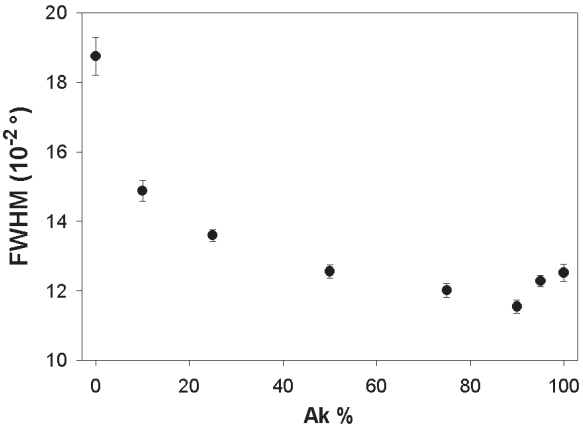

FIGURE 10. Variation of the observed peak width across the åk-ge join as obtained from powder synchrotron XRD on samples S2.

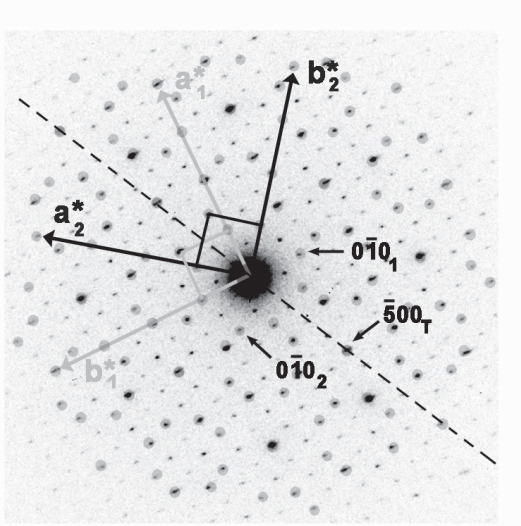

FIGURE 11. [001] electron diffraction pattern of $åk_{08}$ showing superlattice reflections due to twinning. The dark disks have been added to mark reflections belonging to the individual reciprocal lattices (reflections with subscripts 1 and 2), the reciprocal unit cells of which are drawn in gray and black. It must be recalled that these are the only visible reflections if a twinned crystal is analyzed with XRD. The subscript T stands for the twin lattice.

if the contact surface is not normal to the $(001)_I$ plane. If this is the case, then by observing the twin oriented in [001], there is a chance to have a superposition of the two individuals along the optic axis. Therefore, the electrons can be first diffracted by one individual and then by the other. Since electron scattering is stronger than X-ray scattering, this double diffraction is a usual phenomenon. Geometrically, an electron that has undergone a diffraction event in both individuals leaves the sample along a direction corresponding to a linear combination of two reciprocal vectors of the different individual reciprocal lattices. This linear combination coincides with a generic $(hk0)_T$ vector of the twin reciprocal lattice and explains why all the $hk0_T$ reflections can be seen. This twinning seems to be a typical characteristic of the melilite structure. It has been observed in all the S1 samples except for pure åk.

In melilite-like structures, an important factor governing the transition to the modulated structure is the relative ionic radius of the cation in T_1 and T_2. The larger the cation in T_1 and the smaller the cation in T_2, the higher is the transition temperature to the normal phase (Röthlisberger et al. 1990). Therefore, in the åk-ge solid solution, the transition temperature decreases with the Mg ↔ Al and Si ↔ Al substitution. In a recent paper (Merlini et al. 2005), this temperature has been estimated to be 250 K for $åk_{75}$ and lower than 50 K for $åk_{54}$. The disappearance of the modulation with the change of composition has been followed in the examined samples using both electron and X-ray diffraction (see Fig. 12). We have evidence that $åk_{95}$ is still modulated at room temperature. In electron diffraction, the intense $hk0$ satellite reflections become weak, but are still visible in $åk_{95}$, but they are undetected by XRD. The $åk_{75}$ samples do not exhibit satellites but single-crystal XRD analysis of large crystals (~250 μm) shows that the satellites are replaced by diffuse rings similar to those observed by Kusaka et al. (2001) at high temperature on $Ca_2CoSi_2O_7$.

DISCUSSION

The structure analysis of the åk-ge solid solution carried out with both XRD and TEM show that, at room temperature, two different regions can be identified in the compositional range. For compositions rich in Mg, the modulation is the main structural feature. This modulation is still present in $åk_{95}$ samples and causes diffuse scattering in $åk_{75}$. For compositions richer in Al, the modulation disappears and the structure becomes more defective. This defectivity can be seen from high-resolution TEM images, from XRD data, from the microanalysis, and from the anomalous behavior of the cell parameters and cation polyhedra. In particular, the smaller size of the T_2 tetrahedron, which affects the anomalous behavior of the *c* cell dimension, can be explained by an excess of Si. The deviation from the ideal melilite composition must be compensated for by cation vacancies, which may be concentrated in the Ca layer. According to melilite stoichiometry, an excess number of *x* Si atoms per formula unit implies ¼*x* vacancies in the Ca site. In the most favorable case (see Table 6 for $åk_{35}$), this means an occupancy of 0.92 for Ca, which can be difficult to detect by the structural analysis. However, the increase of the Ca polyhedral volume going from $åk_{75}$ to $åk_{08}$ can be understood in terms of vacancies in the Ca site. That the Ca site plays some important role in the defectivity is confirmed also by the high value of d_{max} for ge, which is almost the same as in åk, and by the difference in its trend with respect to the O atoms whose d_{max} decreases from åk to ge. The Ca d_{max} instead stays constant in the interval $åk_{75}$-$åk_{08}$ (see Fig. 7), revealing the superposition of two phenomena: (1) the disappearance of the modulation, and (2) the increase of the number of defects in the structure. These effects are balanced in the middle of the solid solution, whereas one effect dominates over the other close to the end-members. The composition $åk_{50}$ therefore seems to be the saddle point between a modulation region and a defective region. It must be noticed that, for compositions richer in Al than

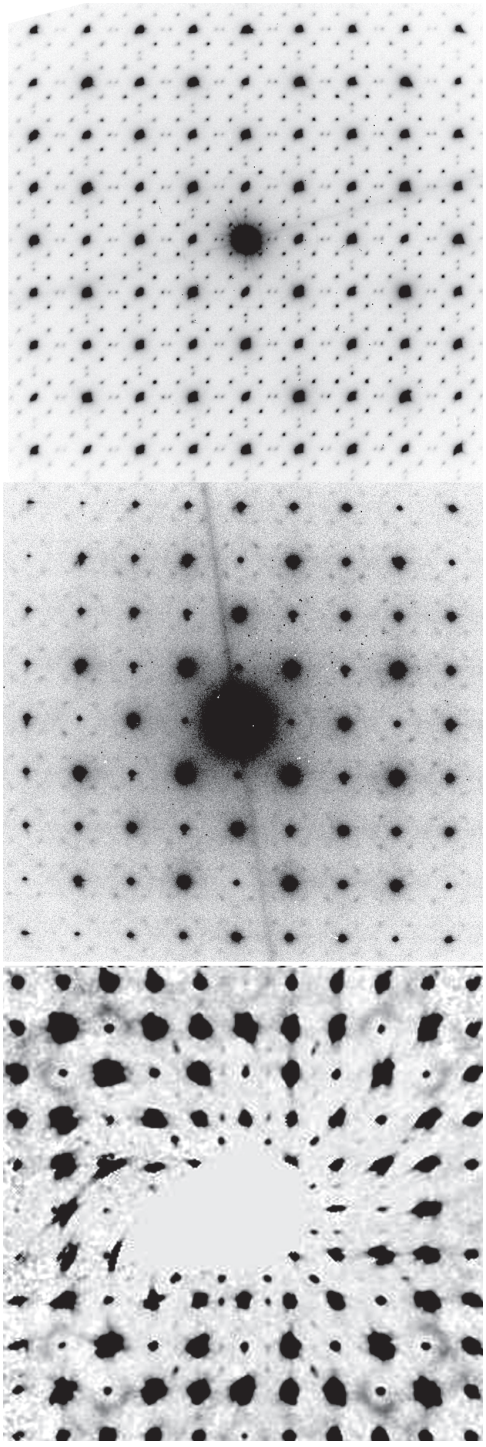

FIGURE 12. [001] reciprocal lattice planes of åk, $åk_{95}$, and $åk_{75}$. (**top**) [001] electron diffraction pattern of åk with characteristic strong two-dimensional modulation. (**middle**) [001] electron diffraction pattern of $åk_{95}$. Weak satellite spots are still visible. (**bottom**) Reconstruction of the [001] reciprocal lattice plane of a relatively large crystal (~300 μm) of $åk_{75}$, as obtained from data collected with a single-crystal X-ray diffractometer equipped with CCD detector. The satellites have completely disappeared but some of them have been replaced by annular diffuse scattering.

$åk_{50}$, Al-O-Al bonds between AlO_4 tetrahedra are not avoidable. These kinds of bonds are unfavorable among silicates if the Al/Si distribution can be arranged to avoid it, i.e., according to the "Loewenstein rule" (Loewenstein 1954). Even if melilite-like T_3O_7 tetrahedral layers seem to escape this rule, it is reasonable to assume that the formation of these Al-O-Al bonds can create local instability in the structure, which tries to react by forming non-stoichiometric melilites with an excess of Si. Therefore, the change in the structural behavior of the solid solution occurs at the $åk_{50}$ composition, and the defectivity in the crystals increases on approaching the ge end-member. Moreover, the only structure showing an Al_3O_7-melilite-like layer, $5CaO\ 3Al_2O_3$, is known to be metastable (Vincent and Jeffery 1978). The unusual twinning by reticular polyholohedry seems to be a common feature in the entire solid solution; therefore it must be related mainly to the topology of the structure and not to fine structural details.

ACKNOWLEDGMENTS

We thank Andrea Migliori of IMM-CNR for assistance during TEM measurements, Carlo Meneghini and all the staff of GILDA beamline at ESRF for technical assistance during synchrotron radiation diffraction experiments and Carla De Pol for assistance during EMPA and single-crystal diffraction measurements. Fiorenza Cella and Tiziano Cerulli of the Research and Development Laboratory of Mapei are kindly acknowledged for their help during the synthesis.

We thank Mihály Pósfai, Laurence Garvie, and an anonymous referee for useful scientific remarks and an accurate revision of the text that improved the quality of the paper.

REFERENCES CITED

Armbruster, T., Röthlisberger, F., and Seifert, F. (1990) Layer topology, stacking variation, and site distortion in the melilite related compounds in the system $CaO\text{-}ZnO\text{-}GeO_2\text{-}SiO_2$. American Mineralogist, 75, 847–858.

Bindi, L., Bonazzi, P., and Fitton, J.G. (2001) Crystal chemistry of strontian melilite from nephelinite lava of Mt. Etinde, Cameroon. European Journal of Mineralogy, 13, 121–125.

Bindi, L., Rees, R.H., and Bonazzi, P. (2003) Twinning in natural melilite simulating a fivefold superstructure. Acta Crystallographica, B59, 156–158.

Blessing, R.H. (1995) An empirical correction for absorption anisotropy. Acta Crystallographica, A51, 33–38.

Charlu, T.V., Newton, R.C., and Kleppa, O.J. (1981) Thermochemistry of synthetic $Ca_2Al_2SiO_7$ (gehlenite)- $Ca_2MgSi_2O_7$ (åkermanite) melilites. Geochimica and Cosmochimica Acta, 45, 1609–1617.

Dapiaggi, M., Gemmi, M., Proverbio, M., and Artioli, G. (2002) Evidence of a superstructure in selected members of synthetic åkermanite gehelenite solid solution. Proceedings of XXXII Congress of Associazione Italiana di Cristallografia. 24th–27th September 2002, Bressanone, Italy.

Deer, W.A., Howie, R.A., and Zussman, J. (1992) An introduction to the Rock-Forming Minerals, 2nd ed. Longman, London.

Giuli, G., Bindi, L., and Bonazzi, P. (2000) Rietveld refinement of okayamalite, $Ca_2SiB_2O_7$: structural evidence for the B/Si ordered distribution. American Mineralogist, 85, 1512–1515.

Hammersley, A.P., Svensson, S.O., Hanfland, M., Fitch, A.N., and Häusermann, D. (1996) Two-dimensional detector software: From real detector to idealized image or two-theta scan. High Pressure Research, 14, 235–248.

Hemingway, B.S., Evans, H.T. Jr., Nord, G.L. Jr., Haselton, H.T. Jr., Robie, R.A., McGee, J.J. (1986) Åkermanite: phase transitions in heat capacity and thermal expansion, and revised thermodynamic data. Canadian Mineralogist, 24, 425–434.

Kimata, M. and Ii, N. (1981) The crystal structure of synthetic åkermanite, $Ca_2MgSi_2O_7$. Neues Jahrbuch fr Mineralogie (Abhandlungen), H1, 1–10.

Kimata, M. and Ohashi, H. (1982) The crystal structure of synthetic gugiaite, $Ca_2BeSi_2O_7$. Neues Jahrbuch fr Mineralogie (Abhandlungen), 143, 210–222.

Kusaka, K., Hagiya, K., Ohmasa, M., Okano, Y., Mukai, M., Iishi, K., and Haga, N. (2001) Determination of structures of $Ca_2CoSi_2O_7$, $Ca_2MgSi_2O_7$ and $Ca_2(Mg_{0.55}Fe_{0.45})Si_2O_7$ in incommensurate and normal phases and observation of diffuse streaks at high temperature. Physics and Chemistry of Minerals, 28, 150–166.

Larson, A.C. and Von Dreele, R.B. (1988) Laur. 86-748, Los Alamos National Laboratory, Los Alamos, New Mexico.

Loewenstein, W. (1954) The distribution of aluminum in the tetrahedra of silicates and aluminates. American Mineralogist, 39, 92–96

Louisnathan, S.J. (1969). Refinement of the crystal structure of Hardystonite,

$Ca_2ZnSi_2O_7$. Zeitschrift für Kristallographie, 130, 427–437.
——— (1970). The crystal structure of the synthetic soda melilite, $CaNaAlSi_2O_7$. Zeitschrift für Kristallographie, 131, 314–321.
——— (1971). Refinement of the crystal structure of a natural gehlenite, $Ca_2Al(Si,Al)_2O_7$. Canadian Mineralogist, 10, 822–837.
Merlini, M., Gemmi, M., and Artioli, A. (2005) Thermal expansion and phase transitions in åkermanite and gehlenite. Physics and Chemistry of Minerals, 32, 189–196.
Nespolo, M. and Ferraris, G. (2004) Applied geminography-symmetry analysis of twinned crystals and definition of twinning by reticular polyholohedry. Acta Crystallographica, A60, 89–95.
Osborn, E.F. and Shairer, J.F. (1941) The ternary system pseudowollastonite-åkermanite-gehlenite. American Journal of Science 239, 715–763.
Oxford (2003) Xcalibur CCD System, CrysAlis Software System, Version 1.171, Oxford Diffraction Ltd.
Panina, Z.V., Malinovskii, Yu.A., Kuz'micheva, G.M., and Zharikov, E.V. (1995) X-ray study of microtwinning in crystals of synthetic Cr^{4+}- and B^{3+}-doped gehlenite, $CaAl(AlSi)O_7$. Crystallography Reports, 40, 593–597.
Peng, C.J., Tsao, R.L., and Chou, Z.R. (1962) Gugiaite $Ca_2BeSi_2O_7$, a new beryllium mineral and its relation to the melilite group. Scientia Sinica, 11, 977–988.
Petricek, V. and Dusek, M. (2000) JANA2000. Institute of Physics, Praha, Czech Republic.
Röthlisberger, F., Seifert, F., and Czank, M. (1990) Chemical control of the commensurate-incommensurate phase transition in synthetic melilites. European Journal of Mineralogy, 2, 585–594.
Seifert, F., Czank, M., Simons, B., and Schmahl, W. (1987) A commensurate-incommensurate phase transition in iron bearing åkermanites. Physics and Chemistry of Minerals, 14, 26–35.
Smith, J.V. (1953) Reexamination if the crystal structure of melilite. American Mineralogist, 38, 643–661.
Swainson, I.P., Dove, M.T., Schmahl, W., and Putnis, A. (1992) Neutron powder diffraction study of the åkermanite-gehlenite solid solution series. Physics and Chemistry of Minerals, 19, 185–195.
Tamazyan, R., Arnold, H., Molchanov, V., Kuzmicheva, G., and Vasileva, I. (2000) Contribution to the crystal chemistry of rare earth chalcogenides. III. The crystal structure and twinning of $SmS_{1.9}$. Zeitschrift für Kristallographie, 215, 346–351.
Taylor, H.F.W. (1997) Cement chemistry. Thomas Telford Publishing, London.
Vincent, M.G. and Jeffery, J.W. (1978) The crystal structure of pentacalcium trialuminate, $5CaO{\cdot}3Al_2O_3$ Acta Crystallographica, B34, 1422–1428.
Waldbaum, D.R. and Woodhead, J.A. (1975) Thermodynamic and crystallographic properties related to Al-Si-Mg ordering in $Ca_2MgSi_2O_7$-$Ca_2Al_2SiO_7$ melilite crystalline solutions. Fortschritte der Mineralogie, 52, 119–131.
Warren, B.E. (1930) The structure of melilite $(Ca,Na)_2(Mg,Al)(Si,Al)_2O_7$. Zeitschrift für Kristallographie, 74, 131–138.
Wood, J.A. (1988) Chondritic Meteorites and the Solar Nebula. Annual Review of Earth and Planetary Sciences, 16, 53–72.
Yoder, H.S. (1973) Melilite stability and paragenesis. Fortschritte der Mineralogie, 50, 140–173.

Manuscript received July 6, 2006
Manuscript accepted May 31, 2007
Manuscript handled by Laurence Garvie